IEEE Access
Multidisciplinary | Rapid Review | Open Access Journal

Received 6 June 2023, accepted 28 June 2023, date of publication 4 July 2023, date of current version 12 July 2023.

Digital Object Identifier 10.1109/ACCESS.2023.3292116

RESEARCH ARTICLE

An Out-of-Focus Image Calibration Method Based on Accurate Positioning of Concentric Circle Projection Center

ZONGYING YU[1], GONGTIAN SHEN[2], ZHANGYAN ZHAO[1], ZHANWEN WU[2], AND YUAN LIU[2]

[1]School of Transportation and Logistics Engineering, Wuhan University of Technology, Wuhan 430063, China
[2]Key Laboratory of Special Equipment Safety and Energy-Saving for State Market Regulation, China Special Equipment Inspection and Research Institute, Beijing 100029, China

Corresponding authors: Gongtian Shen (shengongtian@csei.org.cn) and Zhangyan Zhao (zzy63277@163.com)

This work was supported by the Ministry of Science and Technology, National Key Research and Development Program of China, under Grant 2022YFC3005102.

ABSTRACT During camera calibration, the plane target image is required to occupy most of the whole image, and the focused image is also needed. It is difficult to satisfy these conditions in large-scale structural vision measurement. Therefore, it is very important to explore a camera calibration method with a small calibration board for a large field of view. This paper proposed an out-of-focus image calibration method based on the accurate positioning of concentric circular projection center, which is not limited by the camera's field of view and can overcome the influence of out-of-focus image on camera calibration. The proposed method consists of three parts: adaptive blurred circle image enhancement, accurate positioning of concentric circle projection center and camera calibration of concentric circle center point array. The simulation results show that under different Gaussian blur kernel radius conditions, the proposed accurate positioning method of the concentric circle projection center has better robustness. When Gaussian kernel radius $K = 40$, the positioning accuracy of the proposed method is improved by 41.88%. In the real image experiment, the internal parameters of the camera in the heavy defocus image have similar results to the Zhang's calibration method in the focused image. Both simulation and real image experiments show that the proposed method can realize the calibration of large targets with a small plane calibration board.

INDEX TERMS Concentric circles, camera calibration, defocus image, image enhancement.

I. INTRODUCTION

At present, with the continuous improvement of structural measurement accuracy and the reduction of cost based on vision, the target of structural three-dimensional deformation measurement based on vision is rapidly developing towards large scale [1], [2], [3], [4]. Camera calibration is a bridge between world coordinates and image coordinates, and the calibration accuracy directly affects the measurement accuracy. The traditional camera calibration method is the main method in the visual measurement of large structures. The traditional calibration method needs to use a calibration object with known size or space points (feature points). For example, using total station to determine the coordinates of multiple points on the measured object, or making a three-dimensional model of known size [5], [6], [7], [8]. Among them, Zhang [9] proposed a method of camera calibration by accurately extracting the coordinate array of feature points with a checkerboard plate of known size. Because of its simple manufacture, flexibility, and high accuracy, it has attracted much attention.

However, Zhang's calibration method requires that the plane target should occupy most of the image, and a clear image must be used at the same time. These requirements are difficult to satisfy in large-scale structural visual measurement. Firstly, it is difficult to manufacture, transport and place

The associate editor coordinating the review of this manuscript and approving it for publication was Shovan Barma.

a large calibration plate that matches the size of the measured structure. Secondly, it is difficult for a small calibration board to occupy most of the image within the depth of field of the camera. Putting the calibration board close to the camera can occupy most of the image, but it will produce a blurred image due to defocus, so it is difficult to accurately extract the coordinates of feature points.

Based on the above analysis, if the accurate coordinate array of feature points can be extracted from the defocused blurred image to achieve accurate camera calibration, then the problem of large-field camera calibration with small calibration board will be solved. Scholars have done a lot of research on this issue. Mainly divided into active method and passive method:

The active method uses the grating image with fixed phase to calibrate the camera. Wang et al. [10] adopted a three-phase shifted circular grating (PCG) array as the calibration target, and extracted the center of PCG by ellipse fitting 2π phase points when the target was basically blurred. Cai et al. [11] put forward an improved method of three-phase shift, which encodes the feature points into the phase distribution, recovers the phase distribution by using the phase shift method, and extracts the center of the circular grating as the feature points. Choi et al. [12] dynamically changed the size of the circular pattern, and used the accumulated concentric intensity gradient to identify the local maximum point as the feature point. Bell et al. [13] used a digital display to generate a strip pattern with the carrier phase encoded by feature points, and then recovered the feature points of the blurred image by the corresponding demodulation method. The above methods improve the robustness of feature point location in defocused images. However, the calibration board can't be printed and produced, and it needs the help of a monitor, which is easily influenced by outdoor light sources.

The passive method is to use blur model to eliminate image blur. Baba et al. [14] developed a method to determine the position and width of blur features from multiple blurred edges detected in the blurred image of checkerboard calibration board, and combined with the camera model of thin lens to estimate the internal and external parameters of the camera. Mannan and Langer [15] developed a robust estimation method of absolute blur kernel and relative blur kernel, taking the estimated blur kernel as the point spread function of blurred image, and sharpening the image to identify the feature points of the calibration plate image. Spitschan and Ostermann [16] proposed an angular refinement method for lattice graphs in angular frequency domain. This method uses the symmetry of checkerboard intersection and the periodicity of angular frequency domain when the origin of polar coordinate system is centered on the intersection to determine the position of feature points. The above method uses blurred images to estimate control points, which is simpler and faster than the phase method. However, when the degree of ambiguity is serious, quadrangles and angles cannot provide enough accuracy.

In contrast, circular patterns have abundant geometric properties and high recognition. Meanwhile, the distribution form of pixel intensity of defocused blurred circular image is invariant under ideal conditions, so the circular target has higher accuracy and robustness in camera calibration. The traditional circular calibration board often uses the geometric center coordinates of the circle as the feature points [17], [18], [19]. However, the center of the circle is not the geometric center of the projected ellipse after projection transformation. So in recent years, some scholars have begun to pay attention to using the coordinates of the center point of circular projection as the characteristic point of the calibration board. Yang et al. [20] proposed an intrinsic parameter calibration algorithm using conjugate imaginary intersection of two ellipses projected by two coplanar intersecting circles. Zhao et al. [21] developed a plane target, which consists of two concentric circles and a straight line passing through the geometric center of the circle. The projection center coordinates are obtained based on the invariance of cross ratio. These methods need to know the exact radius of the inner and outer circles in advance, which is obviously difficult to achieve in defocused images. Different from the above-mentioned circle-based projection center extraction method, Hao et al. [22] proposed a simpler method, which calculated the projection center by using the intersection of the geometric center of the circle and the tangent of the circle. This method does not need to know the radius of the circle. However, this method only uses the tangent intersection of one side of the circle to calculate, which is easily affected by the circle fitting error.

On the basis of the above analysis, this paper proposed a camera calibration method that is not limited by the target size. This method only uses a small concentric circle array calibration board to calibrate the camera near the camera, as shown in FIGURE 1. Firstly, a plane plate with concentric array is designed and manufactured as a plane target for camera calibration. Then the adaptive blurred circle image enhancement method is used to reduce the blur degree of the image and sharpen the edge of the image. Finally, based on the projective geometric properties and geometric constraint model, the method of extracting the center point of concentric circle projection is proposed, and the extracted array of concentric circle projection center points in the calibration board is used to calibrate the internal parameters of the camera. The simulation results show that with the increase of Gaussian blur kernel radius, the image blur degree becomes larger and larger. The projection center error of concentric circle extraction also changes constantly. But that propose method is least affected. In the simulation experiment, when the maximum blur kernel radius is $k = 40$, the positioning accuracy of the proposed method is improved by 41.88%. The experimental results of real images show that the camera internal parameters in focused images are almost the same as those in Zhang's calibration method. In different defocus distances, the internal parameters of the camera are also similar to those in the focused image.

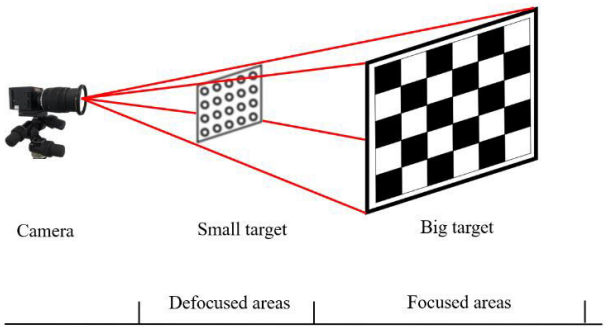

FIGURE 1. Defocus camera calibration.

The remainder of the paper is organized into the following sections: Section II provides the theoretical background of the proposed method. Section III describes the detailed process of the proposed method. Section IV carries out simulation and physical experiments to verify the effectiveness of the proposed method. Conclusions are given in Section V.

II. THEORETICAL BACKGROUNDS

A. PINHOLE CAMERA MODEL

In the ideal pinhole camera model, the transformation process of the world coordinate system, camera coordinate system, image coordinate system and pixel coordinate system is essentially a rigid body transformation, perspective projection and digital image imaging process [23]. As shown in FIGURE 2, $O_W - X_W Y_W Z_W$ represents the world coordinate system, $O_C - X_C Y_C Z_C$ represents the camera coordinate system, $O_I - X_I Y_I$ represents the image coordinate system, and $O_P - X_P Y_P$ represents the pixel coordinate system.

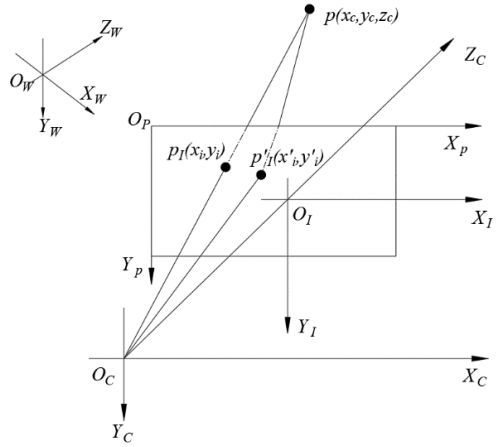

FIGURE 2. Pinhole camera model.

Suppose there is a point p in the world coordinate system, and the corresponding point coordinates in the world coordinate system and the camera coordinate system are $p_w = (X_w, Y_w, Z_w)^T$ and $p_c = (x_c, y_c, z_c)^T$. Then, the conversion relation of point p from the world coordinate system to the camera coordinate system is:

$$\begin{bmatrix} x_c \\ y_c \\ z_c \end{bmatrix} = R \begin{bmatrix} X_w \\ Y_w \\ Z_w \end{bmatrix} + T. \tag{1}$$

where R and T are 3×3 rotation matrix and 3×1 translation matrix, respectively. Homogeneous coordinates can be expressed as:

$$\begin{bmatrix} x_c \\ y_c \\ z_c \\ 1 \end{bmatrix} = \begin{bmatrix} R & T \\ 0^T & 1 \end{bmatrix} \begin{bmatrix} x_w \\ y_w \\ z_w \\ 1 \end{bmatrix}, \tag{2}$$

$$R = \begin{bmatrix} r_1 & r_2 & r_3 \\ r_4 & r_5 & r_6 \\ r_7 & r_8 & r_9 \end{bmatrix}, \quad T = \begin{bmatrix} T_x \\ T_y \\ T_z \end{bmatrix}. \tag{3}$$

The homogeneous coordinate expression of the transformation relationship between the point $p_c = (x_c, y_c, z_c)^T$ in the camera coordinate system and the image coordinate system $(x_i, y_i)^T$ is as follows:

$$z_c \begin{bmatrix} x_i \\ y_i \\ 1 \end{bmatrix} = \begin{bmatrix} f & 0 & 0 & 0 \\ 0 & f & 0 & 0 \\ 0 & 0 & 1 & 0 \end{bmatrix} \begin{bmatrix} x_c \\ y_c \\ z_c \\ 1 \end{bmatrix}. \tag{4}$$

where z_c is the scale factor. In fact, the conversion process is much more complicated due to the manufacturing defects and installation defects of the lens. Resulting in nonlinear transformation process in imaging model. The conversion process from ideal image coordinate $p_I = (x_i, y_i)$ to real image coordinate $p'_I = (x'_i, y'_i)$ is as follows:

$$\begin{cases} x'_i = x_i(1+k_1 r^2 + k_2 r^4 + k_3 r^6) + 2k_4 x_i y_i + k_5(r^2 + 2x_i^2) \\ y'_i = y_i(1+k_1 r^2 + k_2 r^4 + k_3 r^6) + 2k_4 x_i y_i + k_5(r^2 + 2y_i^2). \end{cases} \tag{5}$$

where $r^2 = x_i^2 + y_i^2$, k_1 and k_2 are radial distortion coefficients, k_3 is tilt factor, and k_4 and k_5 are tangential distortion coefficients.

The transformation of point p_I from the image coordinate system to the pixel coordinate system is the process of digitizing the image, and the coordinate origin is in the upper left corner of the image. During this transformation, only the coordinate origin and coordinate unit change. Homogeneous coordinate expression is:

$$\begin{bmatrix} x_i \\ y_i \\ 1 \end{bmatrix} = \begin{bmatrix} \frac{1}{dx_i} & 0 & u_0 \\ 0 & \frac{1}{dy_i} & v_0 \\ 0 & 0 & 0 \end{bmatrix} \begin{bmatrix} x'_i \\ y'_i \\ 1 \end{bmatrix}. \tag{6}$$

where (u_0, v_0) is the origin of the image coordinate system, dx_i and dy_i represent how many millimeters the pixels in each row and column represent respectively.

To sum up, the homogeneous coordinate expression of point transformation from the world coordinate system to the

pixel coordinate system is:

$$z_c \begin{bmatrix} x_i \\ y_i \\ 1 \end{bmatrix} = \begin{bmatrix} \frac{1}{dx_i} & 0 & u_0 \\ 0 & \frac{1}{dy_i} & v_0 \\ 0 & 0 & 1 \end{bmatrix} \begin{bmatrix} f & 0 & 0 & 0 \\ 0 & f & 0 & 0 \\ 0 & 0 & 1 & 0 \end{bmatrix} \begin{bmatrix} R & T \\ 0^T & 1 \end{bmatrix} \begin{bmatrix} X_w \\ Y_w \\ Z_w \\ 1 \end{bmatrix} = \begin{bmatrix} f_x & 0 & u_0 & 0 \\ 0 & f_y & v_0 & 0 \\ 0 & 0 & 1 & 0 \end{bmatrix} \begin{bmatrix} r_1 & r_2 & r_3 & T_x \\ r_4 & r_5 & r_6 & T_y \\ r_7 & r_8 & r_9 & T_z \\ 0 & 0 & 0 & 1 \end{bmatrix} \begin{bmatrix} X_w \\ Y_w \\ Z_w \\ 1 \end{bmatrix}. \quad (7)$$

Suppose $A = \begin{bmatrix} f_x & 0 & u_0 & 0 \\ 0 & f_y & v_0 & 0 \\ 0 & 0 & 1 & 0 \end{bmatrix}$, then the above equation can be abbreviated as:

$$z_c \begin{bmatrix} p_i^T \\ 1 \end{bmatrix} = A \begin{bmatrix} R & T \\ 0^T & 1 \end{bmatrix} \begin{bmatrix} P_W^T \\ 1 \end{bmatrix}. \quad (8)$$

Based on the above expressions, f_x, f_y, u_0, v_0, k_1, k_2, k_3, k_4 and k_5 are camera internal parameters. Matrix R and T are camera external parameters. Before using the camera, it is generally necessary to calibrate the internal and external parameters of the camera respectively in order to get more accurate measurement results.

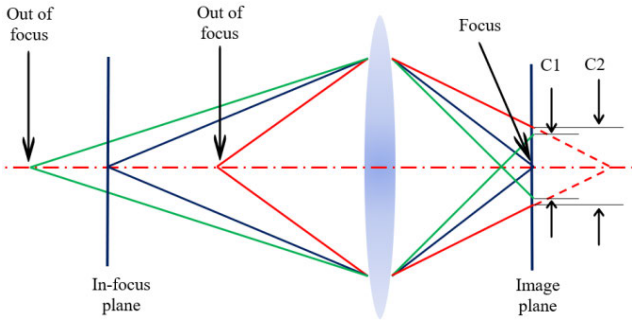

FIGURE 3. Focus and out of focus model.

B. DEFOCUS MODEL

As shown in FIGURE 3, in the thin lens model, the points in the focal plane can converge to one point in the image plane. Out-of-focus points will form a diffuse circular projection on the image plane, which is called a circle of confusion, as shown in C1 and C2 in FIGURE 3. Circles of confusion may appear before and after the focal plane, and the light begins to gather and spread, and the image of the point becomes a blurred circle [24]. The defocused images formed by different points on the measured object are superimposed together, and the blurred image is called defocused image. At the same time, the ideal uniformly distributed circle of confusion in optical system is called point spread function (PSF), which is usually approximate to Gaussian function. Generally speaking, the defocusing process can be modeled as the convolution of a sharp image and PSF.

$$g(x, y) = f(x, y) \otimes h(x, y). \quad (9)$$

where $g(x, y)$ is the light intensity distribution of the imaging position, $f(x,y)$ is the original light intensity distribution of the imaging target, and $h(x,y)$ is the PSF.

Considering that the circle has central symmetry, the position of the center point of the circle will not change after defocusing. At the same time, concentric circles can get the projection center more easily in perspective projection transformation. Therefore, this paper adopts concentric circle to design the calibration plate. The focused concentric circle image becomes a blurred concentric circle image after convolution with PSF, as shown in FIGURE 4(a-b). In this process, the edge of the circle changes from approximate step distribution to one-dimensional 'S' curve distribution.

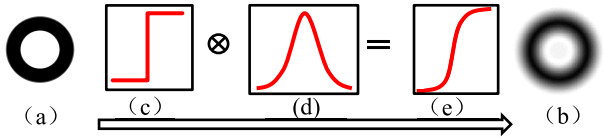

FIGURE 4. Image edge defocus blur: (a) Sharp pattern, (b) Blurred pattern, (c) Step distribution edge, (d)PSF, (e) 'S' curve distribution edge.

Based on the above analysis, we can see that the optical transfer function of the lens can be approximated as a Gaussian function, and its function is equivalent to a low-pass filter. When the defocus is larger, the cut-off frequency of optical transfer function is lower, and the image edge is more blurred. At the same time, the edge of the focused image changes from step distribution to 'S' curve distribution through PSF convolution. In order to accurately extract the edge information of concentric circles, it is necessary to restore the edge of 'S' curve distribution to the step edge of the focused image. Therefore, an adaptive image enhancement model is proposed based on the two-dimensional Otsu method.

III. ALGORITHM PRINCIPLES

This paper proposed a camera calibration method which is not limited by the target size. The proposed method consists of three parts: adaptive blurred circle image enhancement, accurate positioning of concentric circle projection center and camera calibration of concentric circle center point array. This method can be calibrated by using a small calibration board in the defocusing range of the camera, and the effect is similar to that of a large calibration board in the focusing range of the camera.

A. ADAPTIVE BLURRED CIRCLE IMAGE ENHANCEMENT

As we all know, Otsu image segmentation method is an effective image segmentation method. The traditional one-dimensional Otsu method is based on the one-dimensional gray histogram of the image, without considering the spatial correlation between pixels, which leads to poor noise immunity of the algorithm. Compared with one-dimensional Otsu method, two-dimensional Otsu method introduces neighborhood information and makes use of the correlation between pixels to enhance the anti-noise

ability of the algorithm. Similar to other image segmentation methods, image segmentation is easy to cause excessive segmentation of the image and cannot restore the image edge. Which will affect the accuracy of concentric circle edge detection. Therefore, an adaptive image enhancement model is proposed based on the basic principle of the two-dimensional Otsu method [25] and the Sigmoid function. The detailed process is as follows.

Suppose there is an M × N gray image whose gray level is L, the image size of its neighborhood mean is also M × N, and the gray level is also L. Then, the gray value i of a pixel and its neighborhood mean j form a two-dimensional vector (i, j). $f(i,j)$ represents the number of times that the two-dimensional vector (i, j) appears in the histogram, $0 \le i \le L-1$, $0 \le j \le L-1$. The joint probability density $p_{i,j}$ is:

$$P_{i,j} = \frac{f_{(i,j)}}{M \times N}, \tag{10}$$

Also:

$$\sum_{i=0}^{L-1}\sum_{j=0}^{L-1} f_{i,j} = M \times N, \tag{11}$$

$$\sum_{i=0}^{L-1}\sum_{j=0}^{L-1} P_{i,j} = 1. \tag{12}$$

Assuming that s and t are the thresholds in two dimensions of gray level $f(x, y)$ and neighborhood gray level average $g(x, y)$ respectively, the two-dimensional histogram of the image can be divided into four regions: A, B, C and D by this threshold pair, as shown in FIGURE 5:

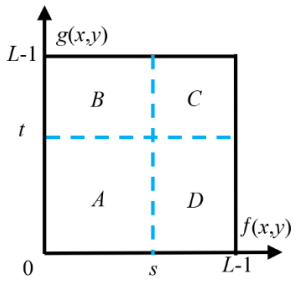

FIGURE 5. Two-dimensional histogram region division.

According to the definition of two-dimensional histogram, the regions A and C on the diagonal in two-dimensional histogram are often regarded as the target region and the background region respectively, while the regions B and D far from the diagonal correspond to noise and edge regions respectively. Assuming that the gray values of image pixels are divided into background and target (represented by C_0 and C_1 respectively), the corresponding probability equation can be obtained:

$$w_0 = \sum_{i=0}^{s}\sum_{j=0}^{t} p_{i,j},\ w_1 = \sum_{i=s+1}^{L-1}\sum_{j=t+1}^{L-1} p_{i,j}. \tag{13}$$

The mean vectors of background and target are as follows:

$$\mu_0 = (\mu_{0i}, \mu_{0j})^T = \left(\sum_{i=0}^{s}\sum_{j=0}^{t} iP_{i,j}, \sum_{i=0}^{s}\sum_{j=0}^{t} jP_{i,j}\right)^T, \tag{14}$$

$$\mu_1 = (\mu_{1i}, \mu_{1j})^T = \left(\sum_{i=s+1}^{L-1}\sum_{j=t+1}^{L-1} iP_{i,j}, \sum_{i=s+1}^{L-1}\sum_{j=t+1}^{L-1} jP_{i,j}\right)^T, \tag{15}$$

The average vector of the whole image is:

$$\mu_T = (\mu_{Ti}, \mu_{Tj})^T = \left(\sum_{i=0}^{L-1}\sum_{j=0}^{L-1} iP_{i,j}, \sum_{i=0}^{L-1}\sum_{j=0}^{L-1} jP_{i,j}\right)^T. \tag{16}$$

The probability of B and D parts in the image is relatively small, so the B and D parts are ignored in the two-dimensional Otsu method. That is:

$$w_0 + w_1 \approx 1 \text{ and } \mu_T \approx w_0\mu_0 + w_1\mu_1. \tag{17}$$

The measures of dispersion between class A and class C is defined as:

$$S_B(s,t) = w_0\left[(\mu_{0i} - \mu_{Ti})^2 + (\mu_{0j} - \mu_{Tj})^2\right] + w_1\left[(\mu_{1i} - \mu_{Ti})^2 + (\mu_{1j} - \mu_{Tj})^2\right], \tag{18}$$

The threshold (s', t') when $S_B(s, t)$ in (18) reaches the maximum value is the optimal segmentation threshold, that is:

$$(s', t') = \arg\max\{S_B(s,t)\}, \quad s' \ge 0, t' \le L-1. \tag{19}$$

Because the traditional two-dimensional Otsu ignores the regions B and D, the edge position of the image is distorted. In this paper, an adaptive image enhancement algorithm based on two-dimensional Otsu is proposed. In this algorithm, the influences of regions B and D are considered.

The adaptive image enhancement algorithm also adopts the above two-dimensional histogram construction method. The difference is that the adaptive image enhancement algorithm not only considers the target area A and the background area C. Noise and edge areas B and D are also considered. In order to restore the image edge more truly, instead of changing the gray value of pixels to 0 or 1 like image segmentation. In this paper, sigmoid function is used to enhance the gray value of pixels in the target area and edge area respectively, while reducing the gray value of pixels in the background area. Sigmoid function, also known as S function or Logistic function, is a continuous, smooth and strictly monotonous threshold function, as shown in FIGURE 4(e). The mathematical model is:

$$f(x) = \frac{1}{1 + e^{-x}}. \tag{20}$$

where x is the gray value of the pixel. According to the properties of Sigmoid function, the range of $f(x)$ is (0,1), and it has very good symmetry. The main steps of the proposed adaptive image enhancement method include:

Step1: According to the traditional two-dimensional Otsu, the optimal thresholds s and t of the gray level $f(x, y)$ of the image and the neighborhood gray level mean value $g(x, y)$ are obtained.

Step2: The two-dimensional histogram of image pixel gray level is divided into four regions: A, C, B and D by using thresholds s and t. Where areas A and C are target areas and background areas, and the range (v_1, v_2) of pixel gray values in the target area is calculated. Save the pixel gray values and pixel coordinate positions of these two areas.

Step3: Because of the uncertainty of the gray value of noise pixels and the blurring of out-of-focus image edges, the pixel values of noise area B and edge area D penetrate each other, and image noise and image edge pixels cannot be effectively distinguished. Therefore, in this method, one-dimensional Otsu [26] is used to calculate the global threshold th of B and D regions. A new target region A'(edge region) and a new background region C'(noise region) in the two-dimensional histogram of the image are obtained.

Step4: A' and C' calculated in Step3 are processed in the next step. Firstly, the gray values of pixels in C' area are replaced by the gray median values of all pixels in the area to eliminate the noise in the image. Then, the range (v_3, v_4) of pixel gray values in the A' region is calculated. Finally, the Sigmoid function is used to map (v_3, v_4) into (v_1, v_2), as shown in equation (21).

$$(v_3, v_4) \overset{f(x)=\frac{1}{1+e^{-x}}}{\rightarrow} (v_1, v_2). \tag{21}$$

After the above processing, the image of defocused blurred circle can be restored well. Of course, repeating the above steps 3 and 4 can further restore the edge of the circle. The proposed method can automatically select the threshold value, and map the pixel gray value of the edge area to the target area of the global image through the Sigmoid function which conforms to the image edge structure. Compared with other methods, it is simple to realize and has high image restoration.

B. DEVIATION ANALYSIS OF CIRCLE CENTER

As we all know, a circle becomes an ellipse on the imaging plane after projection transformation [27]. After the projection transformation, the center of the circle is not the center of the ellipse in the image, but has a deviation [28]. As shown in FIGURE 6, the circle in Π_1 plane is transformed by projection to form an ellipse in Π_2 plane. P′ is the center of the ellipse, and line segment m′n′ is the diameter passing through point P′. In the camera coordinate system O_C-$X_C Y_C Z_C$, extended straight lines m′O_C and n′O_C intersect at points m and n respectively. The point P is the center of the circle and mn is the diameter of the circle.

Suppose that when line mn is parallel to line m′n′, then $\Delta mnO_C \backsim \Delta m'n'O_C$. And because mp = np, so m′p′ = n′p′. However, in the process of pinhole imaging, the image plane of the camera cannot be absolutely parallel to the object plane, so m′p′≠n′p′. Therefore, the geometric center of the ellipse

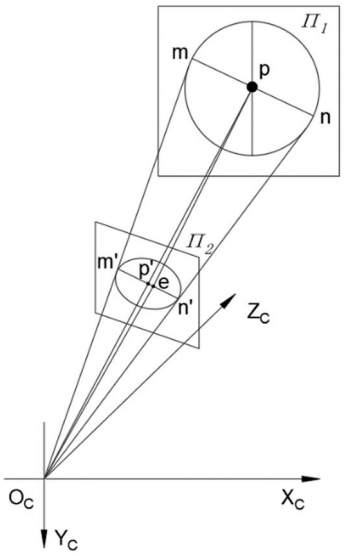

FIGURE 6. Circle projection transformation.

formed by the projection transformation of the circle is not the projection center of the circle, but has a deviation, as shown by point e in FIGURE 6.

Assume that there is a space circle whose center is set at the origin of the world coordinate system, then the equation of the space circle is:

$$\begin{cases} X = R\cos\theta_i \\ Y = R\sin\theta_i \\ Z = z_0. \end{cases} \tag{22}$$

where R is the radius of the space circle, and θ_i is the angle between the line connecting the ith edge point on the circle to the origin and the x axis. The equation of the center of the space circle after projection transformation is:

$$\begin{cases} x = f\dfrac{r_1X + r_2Y + r_3Z + T_x}{r_7X + r_8Y + r_9Z + T_y} \\ y = f\dfrac{r_4X + r_5Y + r_6Z + T_y}{r_7X + r_8Y + r_9Z + T_z}. \end{cases} \tag{23}$$

where f is the focal length of the camera and $r_i (i = 1, \ldots, 9)$ is the rotation angle. T_x, T_y, T_z are translation distances. Assume that the origin of the world coordinate system is at the center of the space circle. Equation (23) can be simplified as:

$$\begin{cases} x = f\dfrac{T_x}{T_y} \\ y = f\dfrac{T_y}{T_z}. \end{cases} \tag{24}$$

In the space circle image, it is assumed that the geometric center coordinate of the ellipse is (x_e, y_e). Therefore, the deviation between the geometric center of the ellipse and the projection center is:

$$\begin{cases} \Delta x = x - x_e \\ \Delta y = y - y_e. \end{cases} \tag{25}$$

According to the above analysis, the space circle will become an ellipse after projection transformation. Moreover, the center of space circle is not the geometric center of ellipse after projection transformation, and there will be some deviation.

Based on the above analysis, the projection center is proposed as the feature point of the target image in this study. In order to quickly calculate the projection center of the circle, concentric circles are chosen as the target patterns in this paper.

C. ACCURATE POSITIONING OF PROJECTION CENTER

Before calculating the projection center, the ellipse in the image is fitted by Lu et al. [29]. According to deviation analysis of circle center, two ellipses are formed after the perspective projection transformation of concentric circles, and the geometric centers of the ellipses are not at the same point. Yang et al. [30] confirmed that the geometric centers of two ellipses are on the same straight line as the projection centers of concentric circles.

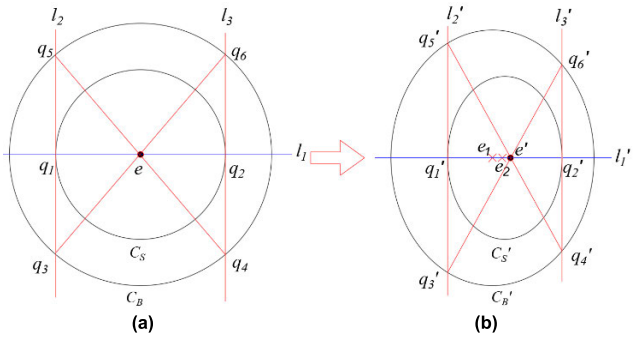

FIGURE 7. Concentric circle projection center positioning: (a) Perfect circle, (b) projection of a circle.

As shown in FIGURE 7(a), the straight line l_1 is a straight line passing through the center of a concentric circle and intersecting the small circle (C_S) at points q_1, q_2 respectively. Make the tangents l_2 and l_3 of the small circle (C_S) through q_1, q_2 respectively, then there must be $l_2//l_3$. Lines l_2 and l_3 intersect the big circle (C_B) at points q_3, q_5, q_4 and q_6 respectively. Cross connecting points q_4, q_5 and q_3, q_6 respectively. Then, the intersection e must be the center of a concentric circle.

According to the photographic invariance in projective geometry, a straight line is still a straight line after projection. The tangent of the circle is still the tangent of the projected ellipse after projection. Parallel lines are still parallel lines after projection. For the point on a straight line, its projection point is still on the projection line. In the projection of concentric circles, the geometric center line l_1' of the two projection ellipses intersects the small ellipse (C_S') at points q_1' and q_2'. Make two tangents l_2' and l_3' of a small ellipse through points q_1' and q_2', then $l_2'//l_3'$. Lines l_2' and l_3' intersect the big ellipse (C_B') at points q_3', q_5', q_4' and q_6' respectively. Cross connecting points q_4', q_5' and q_3', q_6' respectively. The intersection e' is the projection center of concentric circle, as shown in FIGURE 7(b). Similarly, the above content shows that the projection centers of concentric circles are on straight lines l_1', $l_{q3'q6'}$ and $l_{q4'q5'}$ at the same time.

The equations of C_S and C_B are

$$\begin{cases} \phi_S(x) \equiv xE_Sx^T = 0 \\ \phi_B(x) \equiv xE_Bx^T = 0. \end{cases} \tag{26}$$

If the homogeneous coordinates of q_1' and q_2' are $\tilde{x}_S$ and $\tilde{x}_B$ respectively, then the equations of lines l_2' and l_3' are:

$$l_2' = E_S \cdot (\tilde{x}_S)^T \text{ and } l_3' = E_B \cdot (\tilde{x}_B)^T. \tag{27}$$

Points q_3' and q_5' are the intersections of straight line l_2' and big ellipse (C_B'), and points q_4' and q_6' are the intersections of straight line l_3' and big ellipse (C_B'). Connect points q_3', q_6' and q_4', q_5' respectively to obtain two straight lines $l_{q3'q6'}$ and $l_{q4'q5'}$. Homogeneous coordinates of the center point e' of concentric circle projection are:

$$e' = l_{q3'q6'} \times l_{q4'q5'}. \tag{28}$$

Because of the error in ellipse fitting, the point e' is often not collinear with the straight line l_1', as shown in FIGURE 8. In order to reduce the influence of errors, the following treatments are carried out. In the process of calculating the projection center of concentric circles, a threshold δ is set. When the distance from point e' to straight line l_1' is less than or equal to the threshold δ, the projection center of concentric circles is e'. When the distance from the point e' to the line l_1' is greater than the threshold δ, the following calculation is required.

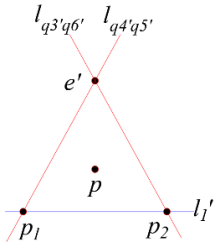

FIGURE 8. Refinement of concentric projection center.

Lines $l_{q3'q6'}$ and $l_{q4'q5'}$ intersect with line l_1' at points p_1 and p_2 respectively. Then this point p is the projection center of concentric circles. The equation is as follows:

$$p = 1/3(e' + p_1 + p_2). \tag{29}$$

A concentric camera calibration board is made based on the above analyses. Because the number of rows and columns of concentric circular array in camera calibration board is known, plane constraints [31] can be used to construct the grid. According to the methods of adaptive blurred circle image enhancement and concentric circle projection center positioning, the projection centers of concentric circle array are calculated respectively. At last, we can use the one-to-one mapping of these projection center point arrays to calibrate the camera.

FIGURE 9. Simulation image: (a) Sharp image, (b) blurred image.

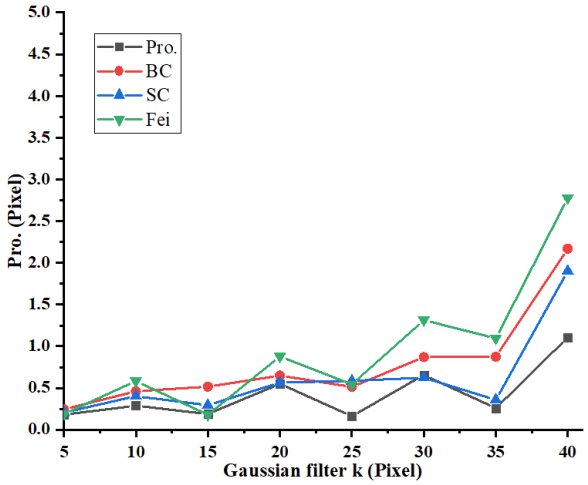

FIGURE 10. Influence of different k on the accuracy.

IV. EXPERIMENTAL VERIFICATION

In this section, the effectiveness and accuracy of the proposed method are verified by experiments. Firstly, the effectiveness of blurred circle image enhancement algorithm and the accuracy of extracting the projection center of concentric circle defocused image is verified by the simulation image. Then, the accuracy of internal parameter calibration of defocus camera is verified by real image experiments. At different defocus distances, the camera is calibrated by the proposed method and the geometric center method of concentric circles and small circles respectively, and the calibration results are compared with the focused checkerboard Zhang calibration method. In the experiment, the camera internal parameters and re-projection errors in the calibration results are used as the judgment basis.

A. EXPERIMENTS WITH SIMULATED IMAGES

Draw concentric circle template with CAD software, and then carry out projection geometric transformation, as shown in FIGURE 9(a). The radii of the small circle and the big circle of concentric circles are 50 mm and 100 mm respectively. Usually, we can get out-of-focus images by point spread function (PSF) convolution of sharp images. PSF is replaced by two-dimensional Gaussian filter. In the experiment, the kernel radius 'k' of two-dimensional Gaussian filters are 5, 10, 15, 20, 25, 30, 35 and 40 respectively. The defocused blurred image when the kernel radius of the two-dimensional Gaussian filter is 40 is shown in FIGURE 9(b). The pixel coordinates of the projection center of concentric circles are extracted by the geometric center method of large ellipse (henceforth referred to as 'BC'), the geometric center method of small ellipse (henceforth referred to as 'SC'), the method of Hao et al. [22] (henceforth referred to as 'Fei') and the proposed method (henceforth referred to as 'Pro.').

The error of concentric circle projection center coordinates extracted by different methods under different two-dimensional Gaussian filter kernels is shown in FIGURE 10. In the simulation experiment, the distance threshold is selected as $\delta = 0.1$. The errors of different methods increase with the increase of k, among which the proposed method has the smallest error and is stable. When $k = 5$, the errors of the proposed method and Fei method are the lowest, which are 0.18074 pixel and 0.18933 pixel respectively, and they are almost the same. The BC has the largest error, with an error of 0.24475 pixel. The SC is the second. When $k = 40$, the error of Fei is the largest, which is 2.77781 pixel; The BC is the second, with an error of 2.16889 pixel. The error of SC is slightly higher than that of the Pro., and the error is 1.90136 pixel. The error of the Pro. is the smallest, and the error is 1.10512 pixel, which is 60.22% higher than that of Fei and 41.88% higher than that of SC.

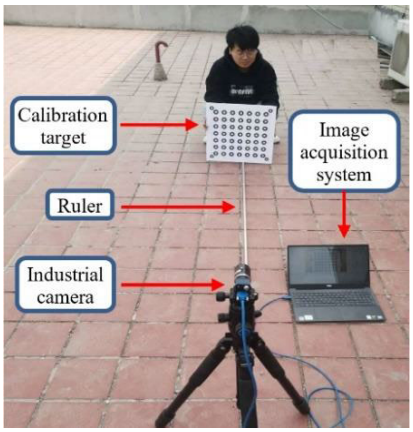

FIGURE 11. Real image experiment.

B. EXPERIMENTS WITH REAL IMAGES

To verify the effectiveness of the proposed method in real images, a single camera calibration experiment is carried out, as shown in FIGURE 11. The resolution of the industrial camera is 5496 × 3672 pixel, and the pixel size is 2.4 μ m. The focal length of the prime lens is 50 mm. The accuracy of a ruler with a length of 10 meters is 1 mm. With the increase of shooting distance, the pattern size should change in proportion. According to four different shooting distances, four 7 × 7 concentric circle pattern plane targets, C1, C2, C3 and C4, were made with an accuracy of 0.01 mm. As shown by the calibration target in FIGURE 11. The specific parameters of the four calibration targets are shown in TABLE 1. Where 'Size' is the side length of the square calibration target,

TABLE 1. Parameters of plane targets with different shooting distance.

Target	Size (mm)	d (mm)	r	R	D (mm)
C1	700×700	100	15	30	7500
C2	376×376	53.7	8	16	4000
C3	282×282	40.3	5	10	3000
C4	188×188	26.9	3	6	2000

TABLE 2. Single camera calibration results of real image experiment.

Method	D (mm)	f_u (mm)	f_v (mm)	u_0 (pixel)	v_0 (pixel)	k_1	k_2	Error (pixel)
Zhang's	7500	49.5818	49.5070	2942.133	1655.325	-0.3428	0.627	0.2535
PC	7500	49.3818	49.3070	2939.054	1649.173	-0.3559	0.609	0.1269
GCS	7500	49.4432	49.4324	2945.448	1657.455	-0.3547	0.630	0.3088
PC	4000	50.2706	50.2668	2936.214	1680.458	-0.3333	0.651	0.2311
GCS	4000	50.5632	50.5426	2955.651	1687.659	-0.3384	0.654	0.3888
PC	3000	49.4923	49.4740	2928.518	1648.164	-0.3523	0.602	0.2981
GCS	3000	49.2144	49.2150	2920.554	1645.223	-0.3554	0.609	0.4654
PC	2000	49.8544	49.8895	2860.452	1635.957	-0.3812	0.644	0.3306
GCS	2000	49.8450	49.8420	2889.317	1642.231	-0.3954	0.645	0.7560

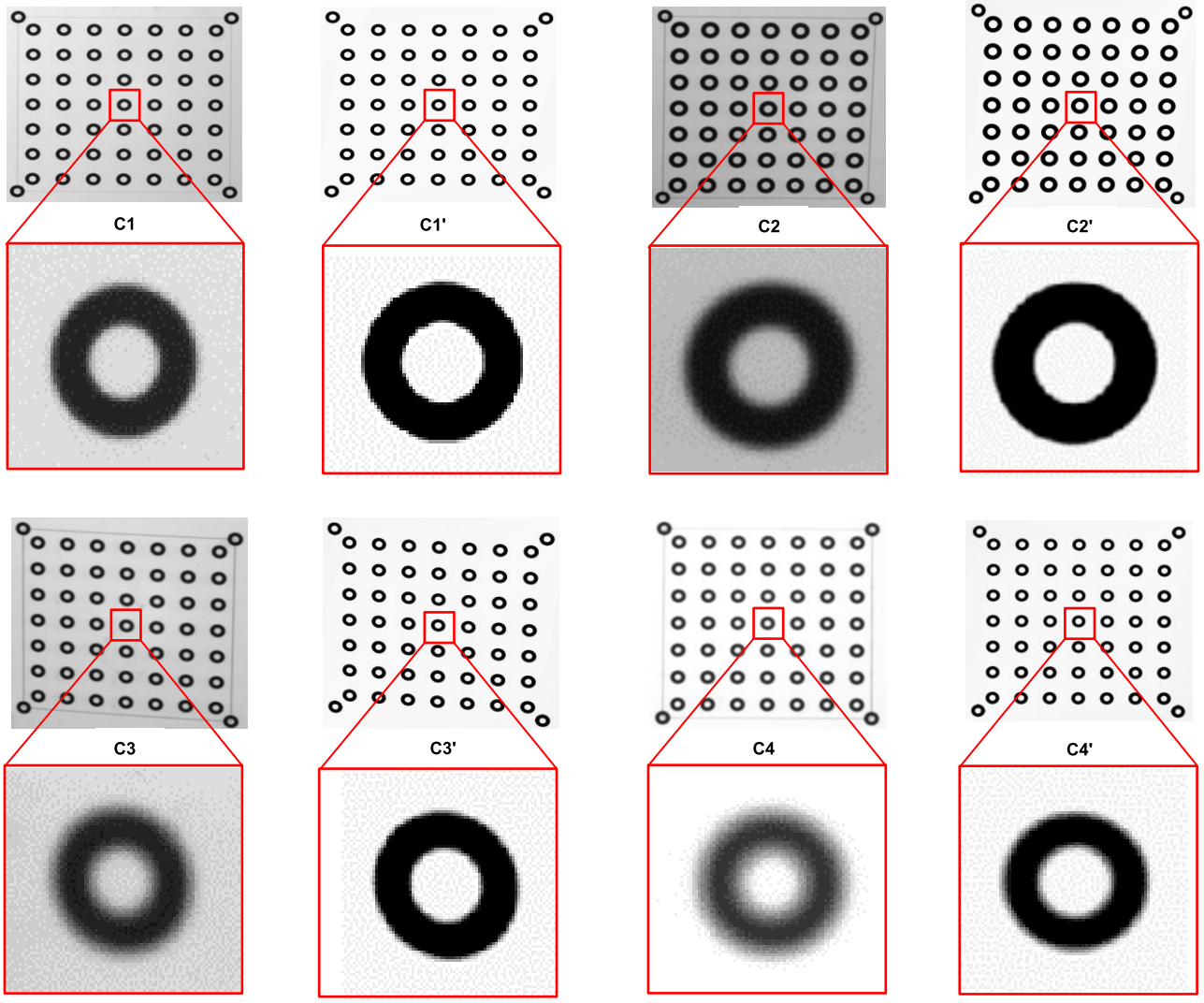

FIGURE 12. Plane target images collected at different shooting distances:C1-C4 real images, C1′-C4′ enhanced image.

'd' is the center distance of each pattern, 'D' is the shooting distance, 'r' is the radius of the small circle, and 'R' is the radius of the big circle.

In the experiment, the concentric circle in the upper left corner is taken as the origin. The camera is installed on a tripod, keeping its inherent parameters unchanged. The thin

lens model shows that different shooting distances will lead to different defocus degrees of images. Put the calibration targets at positions 7500 mm, 4000 mm, 3000 mm and 2000 mm away from the camera respectively. Among them, 7500 mm is in focus, and others are out of focus. In order to ensure the reliability of the experiment, each group of images captures the calibration target images from 20 different viewpoints.

In order to show clearly, the real image schematic diagram in this paper only shows the calibration board. As shown in FIGURE 12. Where C1, C2, C3, and C4 are the real images with different shooting distances, and C1', C2', C3', and C4' are the images enhanced by the proposed adaptive blurred circle image enhancement method. The pictures in the red box are enlarged. The main process of real image experiment is as follows. Firstly, the image is restored by the proposed adaptive blurred circle image enhancement algorithm in different defocus distances. Then, the point array of calibration target images are extracted by using the proposed accurate positioning method of concentric circle projection center (henceforth referred to as 'PC') and the conventional circular geometric center method of small ellipse (henceforth referred to as 'GCS') respectively. Finally, the camera is calibrated by using the extracted point array under the theoretical framework of Zhang's calibration method. Two kinds of camera calibration results of defocused images are compared with Zhang's calibration results of in-focus checkerboard (henceforth referred to as 'Zhang's') [9].

The experimental results are shown in TABLE 2. It can be seen from TABLE 2 that the camera internal parameters obtained by the PC and Zhang's method are almost the same. With the decrease of shooting distance, the re-projection error increases slightly. When the shooting distance is 2000 mm, the maximum re-projection error of PC is 0.3306pixel, which is 0.0771 pixel higher than that of Zhang's calibration method for focused images.

Under different shooting distances, the average focal length error of PC is 32.3% lower than that of GCS. The average error of the principal point of PC is 11.2% lower than that of GCS. The maximum error of k1 in PC and GCS is 11.2% and 15.3% respectively. Among the distortion coefficients of the camera, the tilt factor k_3 and the tangential distortion coefficients k_4 and k_5 are too small, both less than 0.005. Therefore, k_1 and k_2 are sufficient for nonlinear distortion of camera lens. The maximum error of k2 in PC and GCS is 3.8% and 4.8% respectively. The average projection error of PC is obviously lower than that of GCS, which is 0.247 pixels and 0.48 pixels respectively. Experimental results show that the proposed adaptive blurred circle image enhancement algorithm can effectively improve the image sharpness. The PC has achieved higher calibration accuracy than GCS, and the calibration result of PC is closer to the Zhang's.

The results of simulation and real image experiments show that the proposed method can effectively improve the sharpness of defocused images, accurately locate the projection center of concentric circles, and reduce the influence of defocused images on camera calibration. In the visual measurement of large structures, the calibration board can be placed closer to the camera instead of increasing the size of the calibration board.

V. CONCLUSION

In this paper, a camera calibration method that is not limited by the target size is proposed. The camera can be calibrated by placing the plane calibration board closer to the camera, which breaks the target size limitation in the current camera calibration methods. This method consists of three parts: adaptive blurred circle image enhancement, accurate positioning of concentric circle projection center and central point array camera calibration of defocused plane target image. After simulation and real image experiments, the following conclusions are obtained:

(1) The simulation results show that the proposed adaptive blurred circle image enhancement method can effectively reduce the blur degree of out-of-focus images.

(2) The simulation results show that Pro. can accurately extract the concentric projection center, and it has higher robustness in different Gaussian kernel radii. When Gaussian kernel radius k = 40, compared with SC, BC and Fei, the position error of the concentric projection center obtained by Pro. is reduced by 41.88%, 49.05% and 60.22% respectively.

(3) The experimental results of real images show that the proposed method can obtain better camera calibration results at different shooting distances. The experimental results of real images show that under different defocus distances, the average focal length error of PC is 32.3% lower than that of GCS. The average error of the principal point of PC is 11.2% lower than that of GCS.

(4) Although the camera calibration of a large target can be realized by using a small plane calibration board, it is still unable to accurately calibrate the plane target image with more serious blur. And this is the main direction of further research in the future.

REFERENCES

[1] C.-Z. Dong, S. Bas, and F. N. Catbas, "Investigation of vibration serviceability of a footbridge using computer vision-based methods," *Eng. Struct.*, vol. 224, Dec. 2020, Art. no. 111224.

[2] J. Carr, J. Baqersad, C. Niezrecki, and P. Avitabile, "Full-field dynamic strain on wind turbine blade using digital image correlation techniques and limited sets of measured data from photogrammetric targets," *Exp. Techn.*, vol. 40, no. 2, pp. 819–831, Apr. 2016.

[3] B. Pan, L. Tian, and X. Song, "Real-time, non-contact and targetless measurement of vertical deflection of bridges using off-axis digital image correlation," *NDT & E Int.*, vol. 79, pp. 73–80, Apr. 2016.

[4] J. Guo and C. Zhu, "Dynamic displacement measurement of large-scale structures based on the Lucas–Kanade template tracking algorithm," *Mech. Syst. Signal Process.*, vols. 66–67, pp. 425–436, Jan. 2016.

[5] Z.-Y. Hu and F.-C. Wu, "A review on some active vision based camera calibration techniques," *Chin. J. Comput.-Chin. Ed.*, vol. 25, no. 11, pp. 1149–1156, 2002.

[6] W. Qi, F. Li, and L. Zhenzhong, "Review on camera calibration," in *Proc. Chin. Control Decis. Conf.*, May 2010, pp. 3354–3358.

[7] P. Li and J.-N. Wang, "Overview of camera calibration methods," *Shanxi Electron. Technol.*, vol. 4, no. 1, pp. 77–79, 2007.

[8] C.-Z. Dong, O. Celik, and F. N. Catbas, "Marker-free monitoring of the grandstand structures and modal identification using computer vision methods," *Struct. Health Monitor.*, vol. 18, nos. 5–6, pp. 1491–1509, Nov. 2019.
[9] Z. Zhang, "A flexible new technique for camera calibration," *IEEE Trans. Pattern Anal. Mach. Intell.*, vol. 22, no. 11, pp. 1330–1334, Nov. 2000.
[10] Y. Wang, X. Chen, J. Tao, K. Wang, and M. Ma, "Accurate feature detection for out-of-focus camera calibration," *Appl. Opt.*, vol. 55, no. 28, pp. 7964–7971, Oct. 2016.
[11] B. Cai, Y. Wang, K. Wang, M. Ma, and X. Chen, "Camera calibration robust to defocus using phase-shifting patterns," *Sensors*, vol. 17, no. 10, p. 2361, Oct. 2017.
[12] H. Choi, H.-G. Ha, H. Lee, and J. Hong, "Robust control point estimation with an out-of-focus camera calibration pattern," *Pattern Recognit. Lett.*, vol. 143, pp. 1–7, Mar. 2021.
[13] T. Bell, J. Xu, and S. Zhang, "Method for out-of-focus camera calibration," *Appl. Opt.*, vol. 55, no. 9, pp. 2346–2352, 2016.
[14] M. Baba, M. Mukunoki, and N. Asada, "A unified camera calibration using geometry and blur of feature points," in *Proc. 18th Int. Conf. Pattern Recognit. (ICPR)*, vol. 1, Aug. 2006, pp. 816–819.
[15] F. Mannan and M. S. Langer, "Blur calibration for depth from defocus," in *Proc. 13th Conf. Comput. Robot Vis. (CRV)*, Jun. 2016, pp. 281–288.
[16] B. Spitschan and J. Ostermann, "Robust Fourier-based checkerboard corner detection for camera calibration," in *Proc. 23rd Iberoamerican Congr. Pattern Recognit. (CIARP)*, Madrid, Spain. Cham, Switzerland: Springer, 2019, pp. 538–546.
[17] J. Cui, J. Huo, and M. Yang, "The high precision positioning algorithm of circular landmark center in visual measurement," *Optik*, vol. 125, no. 21, pp. 6570–6575, Nov. 2014.
[18] J.-S. Cui, J. Huo, and M. Yang, "The circular mark projection error compensation in camera calibration," *Optik*, vol. 126, no. 20, pp. 2458–2463, Oct. 2015.
[19] J. Heikkila, "Geometric camera calibration using circular control points," *IEEE Trans. Pattern Anal. Mach. Intell.*, vol. 22, no. 10, pp. 1066–1077, Oct. 2000.
[20] L. Yang, L. Guangda, G. Le, C. Xinze, and L. Changying, "Binocular vision calibration method based on coplanar intersecting circles," in *Proc. 10th Int. Congr. Image Signal Process., Biomed. Eng. Informat. (CISP-BMEI)*, Oct. 2017, pp. 1–5.
[21] Y. Zhao, X. Wang, and F. Yang, "Method of camera calibration using concentric circles and lines through their centres," *Adv. Multimedia*, vol. 2018, pp. 1–8, Apr. 2018, doi: 10.1155/2018/6182953.
[22] F. Hao, J. Su, J. Shi, C. Zhu, J. Song, and Y. Hu, "Conic tangents based high precision extraction method of concentric circle centers and its application in camera parameters calibration," *Sci. Rep.*, vol. 11, no. 1, p. 20686, Oct. 2021.
[23] F. Yan, Z. Liu, X. Pan, and Y. Shen, "High-accuracy calibration of cameras without depth of field and target size limitations," *Opt. Exp.*, vol. 28, no. 19, pp. 27443–27458, Sep. 2020.
[24] S. Zhuo and T. Sim, "Defocus map estimation from a single image," *Pattern Recognit.*, vol. 44, no. 9, pp. 1852–1858, Sep. 2011.
[25] J. Zhang and J. Hu, "Image segmentation based on 2D Otsu method with histogram analysis," in *Proc. Int. Conf. Comput. Sci. Softw. Eng.*, vol. 6, Dec. 2008, pp. 105–108.
[26] N. Otsu, "A threshold selection method from gray-level histograms," *IEEE Trans. Syst., Man, Cybern.*, vol. SMC-9, no. 1, pp. 62–66, Jan. 1979.
[27] X. Chen, Y. Hu, Z. Ma, S. Yu, and Y. Chen, "The location and identification of concentric circles in automatic camera calibration," *Opt. Laser Technol.*, vol. 54, pp. 185–190, Dec. 2013.
[28] X. Ying and H. Zha, "An efficient method for the detection of projected concentric circles," in *Proc. IEEE Int. Conf. Image Process.*, vol. 6, Oct. 2007, pp. VI-560–VI-563.
[29] C. Lu, S. Xia, M. Shao, and Y. Fu, "Arc-support line segments revisited: An efficient high-quality ellipse detection," *IEEE Trans. Image Process.*, vol. 29, pp. 768–781, 2020.
[30] S. Yang, M. Liu, S. Yin, Y. Guo, Y. Ren, and J. Zhu, "An improved method for location of concentric circles in vision measurement," *Measurement*, vol. 100, pp. 243–251, Mar. 2017.
[31] J.-Y. Bouguet. (2004). *Camera Calibration Toolbox for MATLAB*. [Online]. Available: http://www.vision.caltech.edu/bouguetj/calib_doc/index.html

ZONGYING YU received the M.S. degree in mechanical design and manufacturing and automation specialty from the University of Science and Technology Beijing, Beijing, China. He is currently pursuing the Ph.D. degree with the Wuhan University of Technology, Wuhan, China. His main research interest includes visual structure health monitoring, detection, and health management.

GONGTIAN SHEN received the B.S. degree in physics and the M.S. degree in metal physics from Wuhan University, Wuhan, China, in 1983 and 1986, respectively, and the Ph.D. degree in material processing engineering from Tsinghua University, Beijing, China.

He is currently a Professor and the Vice Dean of the China Special Equipment Inspection Institute (CSEI), Xiyuan, Chaoyang, Beijing. His research interests include special equipment safety and new technology of nondestructive testing.

ZHANGYAN ZHAO received the B.S. degree in mechanical engineering from Southwest Jiao Tong University, Chengdu, China, and the M.S. and Ph.D. degrees in mechanical engineering from the Wuhan University of Technology, Wuhan, China, in 1991 and 2001, respectively. He is currently a Professor and a Doctoral Supervisor at the Wuhan University of Technology. His research interests include metal structure fault diagnosis and safety evaluation, computer vision, and computer-aided engineering and manufacturing.

ZHANWEN WU received the Ph.D. degree from the Wuhan University of Technology, Wuhan, China, in 2010. He works with the China Special Equipment Inspection and Research Institute, Beijing. His research interests include new technology of special equipment detection and evaluation, condition monitoring, and fault diagnosis technology.

YUAN LIU received the B.S. degree in mechanical engineering from the Jiangxi University of Science and Technology, Ganzhou, China, in 2005, the M.S. degree in mechanical engineering from Guangxi University, Nanning, China, in 2011, and the Ph.D. degree in mechanical engineering from the Wuhan University of Technology, Wuhan, China. His research interests include condition monitoring and health management of special equipment.